JOURNAL OF GUIDANCE, CONTROL, AND DYNAMICS
Vol. 31, No. 3, May–June 2008

Fault Diagnosis of Microscope Satellite Thrusters Using H_∞/H_- Filters

D. Henry*
Université Bordeaux I, 33405 Talence, France

DOI: 10.2514/1.31003

Microscope is a satellite due to be launched in March 2008 (Microscope is undertaken jointly by the Centre National d'Etudes Spatiales, France, the ESA, the Office National d'Etude et de Recherche en Aerospatial, France, and the Côte d'Azur Observatory, France). It has the mission of testing the equivalence principle, which postulates the equality between gravitational mass and inertial mass. This paper addresses the fault diagnosis task of the Microscope thrusters. The faulty situations correspond to thrusters blocking themselves and/or closing when in operation. Two model-based diagnosis schemes based on H_∞/H_- filters are proposed and compared with each other in terms of performances and complexity. Nonlinear simulations show that both schemes are able to detect and isolate faults, despite the presence of measurement noises, measurement delays, sensor misalignment phenomena, and disturbances (i.e., third-body disturbances, J_2 disturbances, atmospheric drag, and solar radiation pressure).

I. Introduction

MICROSCOPE is a satellite due to be launched in March 2008 on a circular, quasi-polar, sun-synchronous orbit at an altitude of 700 km with ascending and descending nodes at 0600 and 1800, respectively. The Microscope experiment is an attempt to test the equivalence principle with a resolution of almost 3 orders of magnitude more than the best tests so far performed on Earth. The idea is to measure the relative acceleration of two masses of different composition in free motion in a drag compensated satellite in orbit in the Earth's gravitational field. The main advantage of a space experiment is that it will eliminate random vibrations of seismic origin, which currently limit laboratory experiments.

To carry out its mission, Microscope combines two rotation motions: the first one is a rotation around the Earth and the second one is a spin rotation. To control its trajectory, Microscope uses the coupling of six ultrasensitive accelerometer sensors, a stellar sensor, and a very precise electric propulsion system composed of 12 field emission electric propulsion (FEEP) thrusters.

The mission can be endangered if a FEEP thruster fault occurs, because the satellite may not compensate for the nongravitational disturbances that are indispensable to the prior conditions for testing the equivalence principle. Such faulty situations can, of course, be diagnosed by operators using telemetry information collected by ground stations. However, the potential lack of communication between the satellite and the ground stations could lead to significant delays, which in turn could lead to the abortion of the Microscope mission. This motivates the development team to manage studies for onboard fault detection and isolation (FDI) solutions. The final goal is to anticipate recovery actions.

There exist many techniques in the FDI literature (see [1–5] for surveys). Some of them use mathematical models of the monitored process. In the aerospace field, different model-based FDI techniques have been considered in the past. Many studies are based on particle filtering-based algorithms (see the nonexhaustive [6–9]). Basically, a particle filter is a Markov chain Monte Carlo algorithm that performs a system state estimation using a set of samples (particles). In Venkateswaran et al. [10], the proposed method is based on an FDI observer combined with a residual weighting matrix. The proposed design procedure involves eigenstructure assignment. In Jensen and Wisniewski [11], directional nonlinear observers are used to detect and isolate faults in small satellites' actuators. The idea is to design the observer gain so that the kth component of the residual changes in a definite direction if and only if a fault occurs in the kth actuator. Other FDI techniques are based on the so-called sliding mode observers [12–14]. The approach consists of performing an estimate of the fault rather than detecting the presence of it through a residual signal. The method could also provide a direct estimate of the fault's size. Some other interesting results are presented in Patton et al. [15]. In this paper, robust dynamic observers, used and organized as a bank of estimators, generate the residual signals. Selected performance criteria indices are also used, together with Monte Carlo robustness tuning and performance evaluation, to provide fault diagnosis solutions.

The majority of the aforementioned methods involves the use of an open-loop model of the monitored system, in spite of the fact that the FDI scheme is placed in a feedback loop. In such situations, it is well known that faults may be covered by control actions, and the early detection of them is clearly more difficult. This motivates the so-called integrated design of control and diagnosis schemes in which robust controllers and fault detectors are designed together by optimizing a set of mixed control and fault detection objectives [16–21]. However, this solution can not be applied here, because the already-in-place attitude and orbit control system unit is certified and thus cannot be removed.

To overcome this problem, the method proposed in Henry and Zolghadri [22,23] is used. The procedure aims to generate a structured residual vector r in the following general form:

$$r(s) = M_y y(s) + M_u u(s) - L(s)\begin{pmatrix} y(s) \\ u(s) \end{pmatrix}, \qquad u(s) = K(s)y(s) \tag{1}$$

where K denotes the controller, M_y and M_u are the two residuals structuring (constant) matrices, and $L(s)$ is a (stable) dynamical filter. The proposed method is developed in a very similar manner as the well-known H_∞/μ robust controller design technique. It consists of jointly designing M_y, M_u, and $L(s)$ such that the effects that faults have on r are maximized in the H_--norm sense while the influence of unknown inputs and model uncertainties in the H_∞-norm sense are minimized. Furthermore, it is shown how robust poles assignment and H_{2g} specifications can be considered.

Other authors have also proposed H_∞/H_- methods for FDI schemes (a good survey/overview can be found in Marcos et al. [24]). The methods can be classified as 1) fault signal estimation-based

Received 13 March 2007; revision received 8 October 2007; accepted for publication 11 December 2007.

*IMS–UMR CNRS 5218, 351 cours de la Libération; david.henry@u-bordeaux1.fr.

approaches (see [24–34]), and 2) residuals generation based-approaches (see [1,22,23,35–41].

Algebraic Riccati equation-based solutions, μ optimization techniques, linear matrix inequality computation solutions, eigenstructure assignment, and genetic algorithms were developed by the authors to derive the solution. However, as already mentioned, the proposed methods do not include the controller actions within the design procedure, and this is a great advantage of the method proposed by Henry and Zolghadri [22,23]. Another great benefit of the approach developed in Henry and Zolghadri [22,23] is that the residuals structuring matrices are jointly designed with, say, the dynamical part of the FDI scheme. Furthermore, the used framework (i.e., the H_∞ framework) makes it easy to include a large range of robustness objectives within the design procedure, for example, against various disturbances, perturbations, and model uncertainties.

The purpose of this paper is to develop and compare two FDI schemes based on the H_∞/H_- fault detection scheme proposed in Henry and Zolghadri [22,23]. The aim is to diagnose Microscope FEEP thruster faults despite the presence of measurement noises, measurement delays, sensor misalignment phenomena, and disturbances (i.e., third-body disturbances, J_2 disturbances, atmospheric drag, and solar radiation pressure). The considered faults to be diagnosed correspond to FEEP thrusters blocking or closing themselves when in operation. Because these faulty situations are the most common in practice, they are of prime interest.

II. Modeling Microscope

Figure 1 shows the general setup of Microscope (for confidential reasons, the numerical values with regard to the satellite geometry and characteristics are omitted). A stellar sensor and three-axes accelerometers allow measurement of the attitude $\Theta(t)$, the angular acceleration $\dot{\varpi}(t)$, and the linear acceleration $\Gamma(t)$. The angular accelerometers and the stellar sensor are placed in the center of mass of the satellite, whereas the linear accelerometers are not. This introduces nonlinearities in the Microscope model output Eq. (22) (seen later). To overcome this problem, a subsystem of the navigation unit, called a "hybridation filter," performs an estimate $\hat{\Gamma}(t)$ of the linear acceleration in the center of mass. The design of the hybridation filter is not considered in this paper.

Another role of the hybridation filter is to perform an estimate $\hat{\Theta}(t)$ of $\Theta(t)$ removing misalignment phenomena and noises on $\Theta(t)$. Then, $\hat{\Gamma}$ and $\hat{\Theta}$ will be used later for the design of the FDI unit. However, we assume that the navigation unit is not perfect and, thus, that there still exists time delays and noises on $\hat{\Theta}(t)$, $\dot{\varpi}(t)$, and $\hat{\Gamma}(t)$.

In terms of actuators, Microscope is equipped with 12 FEEP thrusters dispatched at its angles. These allow for control of the satellite motion. More precisely, the open rate of each FEEP thruster is controlled by the correction loop to maintain the attitude and the linear acceleration to zero and the orbit rotational velocity ϖ_α and the spin rotational velocity ϖ_{spin} to constant values.

A. Modeling the Motion of the Satellite

The equations for the rotational motion of Microscope in the body-fixed axis system (the center of this frame is fixed to the center of mass of Microscope) are derived from the moment vector equation:

$$C = I_s\dot{\varpi} + \varpi \times I_s\varpi \tag{2}$$

where $\times$ denotes the cross product of vectors and I_s is the inertia matrix. C is the moments about the center of mass due to the propulsion and disturbances. $\varpi = (pqr)^T$ is the inertial rotational velocity and $\dot{\varpi}$ is the inertial rotational acceleration. Taking into account the spin rotational velocity ϖ_{spin} of Microscope, the relation between the rotational velocities and the attitude (Cardan) angles $\Theta = (\theta_x\theta_y\theta_z)^T$ is given by [42,43]

$$\begin{pmatrix} p \\ q \\ r \end{pmatrix} = \begin{pmatrix} 1 & 0 & -\sin\theta_y \\ 0 & \cos\theta_x & \sin\theta_x\cos\theta_y \\ 0 & -\sin\theta_x & \cos\theta_x\cos\theta_y \end{pmatrix} \begin{pmatrix} \dot{\theta}_x \\ \dot{\theta}_y \\ \dot{\theta}_z \end{pmatrix} \cdots - \varpi_{\text{spin}} \begin{pmatrix} \cos\theta_y\sin\theta_z \\ \cos\theta_x\cos\theta_y + \sin\theta_x\sin\theta_y\sin\theta_z \\ -\sin\theta_x\cos\theta_z + \cos\theta_x\sin\theta_y\sin\theta_z \end{pmatrix} \tag{3}$$

The indices x, y, and z are classically referred to as the x, y, and z axes of the body-fixed frame. For Microscope, the gravitational forces are compensated for by the Coriolis forces. Thus, the satellite linear acceleration that describes the translational motion is given by the following equation:

$$m\Gamma = F + mg_L \tag{4}$$

where m denotes the mass of Microscope. F is the forces due to the propulsion and disturbances. $\Gamma = (\Gamma_x\Gamma_y\Gamma_z)^T$ is the linear acceleration about the center of mass. g_L also denotes the local gravitational field.

B. Modeling the Navigation Unit and the FEEP Thrusters

As mentioned, the navigation unit is not considered to deliver "perfect" measurements. We assume time delays and noises. The numerical values of the time delays have been determined to be 0.1 s for the $\dot{\varpi}(t)$ and $\hat{\Gamma}(t)$ measurements and 0.5 s for $\hat{\Theta}(t)$. For both the $\dot{\varpi}(t)$ and $\hat{\Gamma}(t)$ measurements, the noises are modeled as coloring signals, that is, they are considered to be the result of filtering Gaussian white noise through a dynamical filter. Experiments were performed to determine these filters (the experiments were performed by a partner of the project and will not be discussed in this paper). They are found to be of an order 6 for the x component and of a second order for both the y and z components. For $\hat{\Theta}(t)$, we assume simply Gaussian white noises on each axis.

The model describing the dynamics of each FEEP thruster is chosen to be simply a first-order transfer $H_{\text{FEEP}}(s)$ with a cutting frequency of 2 rad/s, that is,

$$H_{\text{FEEP}}(s) = \frac{1}{1 + 0.5\ \text{s}} \tag{5}$$

C. Modeling the Control Loop

The control law consists of two second-order linear controllers and a control allocator called a nonlinear iterative pseudoinverse controller (NIPC). Figure 2 illustrates the control law and the NIPC.

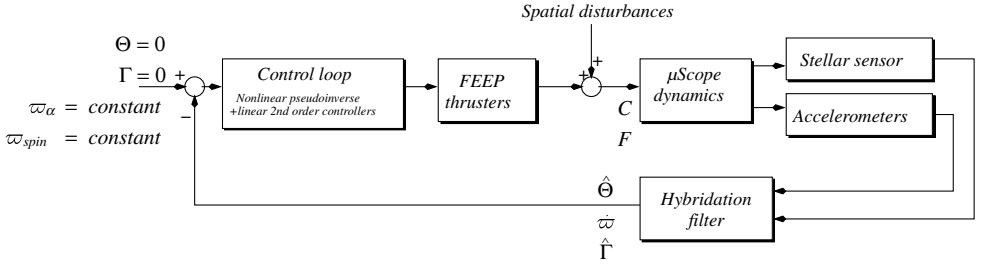

Fig. 1 General setup of Microscope.

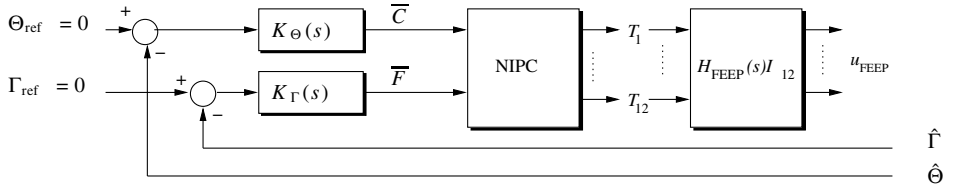

Fig. 2 Control law in Microscope.

The control law allows for the compensation of disturbances that, again, are indispensable to the prior conditions for testing the equivalence principle.

The controller $K_\Theta(s)$ allows the attitude $\Theta(t)$ to be maintained at zero (i.e., $\theta_x = 0$, $\theta_y = 0$, and $\theta_z = 0$) and the controller $K_\Gamma(s)$ has been designed to maintain the linear acceleration $\Gamma(t)$ at zero (i.e., $\Gamma_x = 0$, $\Gamma_y = 0$, and $\Gamma_z = 0$). The NIPC allocator works in such a way that it manages the open rate of each of the 12 FEEP thrusters. Basically, the NIPC consists of the computation of a matrix inverse:

Let T_i be the open rate of the ith thruster. Then, the moments $\bar{C}$ and the forces $\bar{F}$ generated by the FEEP thrusters are given by

$$\begin{pmatrix} \bar{C} \\ \bar{F} \end{pmatrix} = M \begin{pmatrix} T_1 \\ \vdots \\ T_{12} \end{pmatrix} \tag{6}$$

where $M \in \mathbb{R}^{6\times 12}$ is the thruster configuration matrix. The elements of M are the influence coefficients defining how each thruster affects each component of $\bar{C}$ and $\bar{F}$. Thus, the computation of each T_i, $i = 1, \ldots, 12$ can be done using a simple inversion of Eq. (6). Because M has more columns than rows, there exists an infinite number of solutions. However, by minimizing some norm of M, the solution can be made unique, for example, minimum-power NIPC results in $\min \|M\|_2$ and, thus, in the Moore–Penrose matrix computation M^+. The interested reader can refer to Jin et al. [44] and Wiktor [45] for more details.

D. Modeling the Disturbances

The disturbances that affect the satellite motion are considered to be due to four phenomena: magnetic, gravitational, aerodynamic, and solar. In the following subsections, mathematical models of these disturbances are given. The reason for such an interest is that they will be used later to enhance the robustness level of the proposed FDI schemes.

1. *Magnetic Disturbances*

Because the satellite is constructed with magnetic materials, there exists a magnetic moment C_m affecting the satellite motion. Using the bipolar magnetic moment model, this disturbance can be modeled according to

$$C_m = M_m \times \frac{M_0}{r^3}\left(-2\sin\alpha\begin{pmatrix} \sin(\alpha-\theta_{spin}) \\ 0 \\ \cos(\alpha-\theta_{spin}) \end{pmatrix} - \cos\alpha\begin{pmatrix} -\cos(\alpha-\theta_{spin}) \\ 0 \\ \sin(\alpha-\theta_{spin}) \end{pmatrix}\right) \tag{7}$$

where M_m and M_0 are satellite characteristics, r is the orbital radius (i.e., $r = r_{Earth} + 700$ km), and α and θ_{spin} denote the orbit position angle and the spin angle of the satellite, respectively.

2. *Gravitational Disturbances*

Because the gravity center of Microscope does not equal the center of mass, there exists a gravity gradient C_g acting on the satellite. Here, the following model is used for C_g:

$$C_g = \frac{3\mu}{r^3}\begin{pmatrix} \sin(\alpha-\theta_{spin}) \\ 0 \\ \cos(\alpha-\theta_{spin}) \end{pmatrix} \times I_s \begin{pmatrix} \sin(\alpha-\theta_{spin}) \\ 0 \\ \cos(\alpha-\theta_{spin}) \end{pmatrix} \tag{8}$$

where μ is the Earth gravitational constant, that is,$\mu = 3.986005e14$ m^3/s^2.

3. *Aerodynamic Disturbances*

Because of the translational motion of Microscope and due to the atmospheric winds, there exist aerodynamic frictions. Of course, because Microscope orbits at 700 km, these disturbances can be neglected. However, we still consider them in this study.

The aerodynamic forces can be modeled according to

$$F_{aero} = F_{sm} + F_{atmo} \tag{9}$$

F_{sm} models the forces due to the satellite motion in the atmosphere, whereas F_{atmo} models the effects that atmospheric winds have on Microscope. F_{sm} is defined according to

$$F_{sm} = \sum_k \frac{1}{2}\rho(\alpha)S_k|N_k \bullet V_{air}|((N_k \bullet V_{air})(C_t - C_n)N_k + C_t V_{air}) \tag{10}$$

where $\bullet$ denotes the scalar product of vectors. k is used to denote the kth face of the satellite exposed to aerodynamic frictions. $\rho(\alpha)$ is the atmospheric density. It depends on the orbit position angle of the satellite. S_k denotes the surface of the kth face of the satellite, N_k is the kth satellite face normal, and C_t and C_n are the transverse and normal friction coefficients. V_{air} is the air speed vs the satellite and is also defined in the body-fixed coordinates by

$$V_{air} = \frac{\mu}{r}\begin{pmatrix} \sin(\theta_{spin}-\alpha-\pi/2) \\ 0 \\ -\cos(\theta_{spin}-\alpha-\pi/2) \end{pmatrix} \tag{11}$$

Similarly, F_{atm} is defined according to

$$F_{atm} = \sum_k \frac{1}{2}\rho(\alpha)S_k|N_k \bullet V_{atm}|((N_k \bullet V_{atm})(C_t - C_n)N_k + C_t V_{atm}) \tag{12}$$

where V_{atm} is the atmospheric winds speed given by

$$V_{atm} = \frac{2\pi r_{Earth}}{86,400}\cos(\alpha)\begin{pmatrix} \cos(\beta)\cos(\theta_{spin}) \\ -\sin(\beta) \\ \cos(\beta)\sin(\theta_{spin}) \end{pmatrix} \tag{13}$$

where β is the inclination angle of Microscope. The aerodynamic moments acting on the satellite are then directly derived from Eq. (9) following the equation

$$C_{aero} = \sum_k \mathcal{D} \times F_{aero_k} \tag{14}$$

where $\mathcal{D}$ is a vector characterizing the Microscope geometry.

4. *Solar Disturbances*

The last spatial disturbances are due to the impact of the solar radiations that cause a photonic pressure on the satellite. This phenomena manifests itself in two ways: direct solar radiations and

albedo radiations. The two phenomena cause forces and moments that affect the satellite motion. The forces can be modeled according to

$$F_{\text{solar}} = F_d + F_{\text{albedo}} \tag{15}$$

where F_d and F_{albedo} model the forces due to direct solar and albedo radiations, respectively. F_d is defined according to

$$F_d = \sum_k - P_{\text{sol}} S_k |\chi_{\text{sol}} \bullet N_k| (2C_s(\chi_{\text{sol}} \bullet N_k)N_k + (1 - C_s)\chi_{\text{sol}}) \tag{16}$$

where k denotes the kth face of the satellite exposed to the sun. P_{sol} is the solar radiation pressure and C_s is the reflectivity coefficient that characterizes the materials used to build the satellite. χ_{sol} is also defined in the body-fixed coordinates according to

$$\chi_{\text{sol}} = \begin{pmatrix} \cos(\phi + \beta + \pi/2)\cos(\theta_{\text{spin}}) \\ -\sin(\phi + \beta + \pi/2) \\ \cos(\phi + \beta + \pi/2)\sin(\theta_{\text{spin}}) \end{pmatrix} \tag{17}$$

where ϕ denotes the solar declination depending on the season, that is, $-23.27 \text{ deg} < \phi < 23.27$ deg. Similarly, F_{albedo} is defined according to

$$F_{\text{albedo}} = \sum_k - P_{\text{albedo}} S_k |\chi_{\text{albedo}} \bullet N_k| (2C_s(\chi_{\text{albedo}} \bullet N_k)N_k + (1 - C_s)\chi_{\text{albedo}}) \tag{18}$$

where χ_{albedo} is defined in the body-fixed coordinates according to

$$\chi_{\text{albedo}} = \begin{pmatrix} -\sin(\alpha - \theta_{\text{spin}}) \\ 0 \\ -\cos(\alpha - \theta_{\text{spin}}) \end{pmatrix} \tag{19}$$

The moments caused by both direct solar and albedo radiations are given by

$$C_{\text{solar}} = \sum_k \mathcal{D} \times F_{\text{solar}_k} \tag{20}$$

E. Toward a Linear Time-Invariant Model of Microscope

From (2–6) and taking into account the control law, a nonlinear model that describes the overall Microscope system can be derived. In fact, because the hybridation filter is designed to be robust to the local gravitational field [i.e., the term g_L in Eq. (4)], it can be verified that Eqs. (2–6) allow for the definition of the following model (see Figs. 1 and 2 for easy reference):

$$\begin{cases} \dot{x} = f(x, \varpi_{\text{spin}}) + E_1 h(\varpi_\alpha, \varpi_{\text{spin}}) + BMC_P x_P \\ \dot{x}_P = A_P x_P + B_P T \\ \bar{y} = g(x) + E_2 h(\varpi_\alpha, \varpi_{\text{spin}}) + DMC_P x_P \end{cases} \tag{21}$$

$$y_i = e^{-\rho_i s}\bar{y}_i + n_i \tag{22}$$

$$T = M^+ \begin{pmatrix} K_\Theta(s)\hat{\Theta} \\ K_\Gamma(s)\hat{\Gamma} \end{pmatrix} \tag{23}$$

The subscript i is used to denote the ith component of a vector. ρ_i denotes the time delay of the ith measurement coming from the navigation unit, that is, $\rho_i \in \{0.1 \text{ s}; 0.5 \text{ s}\}$. $h(\varpi_\alpha, \varpi_{\text{spin}}) = ((C_{\text{aero}} + C_{\text{solar}} + C_m + C_g)^T (F_{\text{aero}} + F_{\text{solar}})^T)^T$ is the vector related to the moments and forces due to disturbances. The notation $(\varpi_\alpha, \varpi_{\text{spin}})$ is used to keep in mind that the disturbances depend on ϖ_α: $\alpha = \varpi_\alpha t$ and ϖ_{spin}: $\theta_{\text{spin}} = \varpi_{\text{spin}} t$ [see Eqs. (7–20)]. $T = (T_1, \ldots, T_{12})^T$ is the controlled input vector due to the propulsion and $y = (\hat{\Theta}^T \dot{\varpi}^T \hat{\Gamma}^T)^T$ is the measurements vector. n also denotes the associated noises coming from the "imperfect" navigation unit. $x = (pqr\theta_x\theta_y\theta_z)^T$ is the state vector and $g(x)$ and $f(x, \varpi_{\text{spin}})$ are the nonlinear functions depending on x and the spin rotational velocity ϖ_{spin}. B, D, E_1, and E_2 are constant matrices of appropriate dimensions. A_P, B_P, C_P, and x_P are, respectively, the state matrices and the state vector associated with the transfer $H_{\text{FEEP}}(s)$.

With regard to the faults, we are interested in the FEEP thrusters blocking or closing themselves when in operation. Such faults can be modeled in a multiplicative manner according to

$$u^f_{\text{FEEP}}(t) = (I_{12} - \psi)u_{\text{FEEP}}(t), \qquad \psi = \text{diag}\{\psi_1, \psi_2, \ldots, \psi_{12}\} \tag{24}$$

where ψ_i, $i = 1, \ldots, 12$ are unknown (see [2–5,46] for a discussion about the fault classification). I_{12} denotes the identity matrix of dimension 12 and u_{FEEP} is the thrust signal applied to the satellite (see Fig. 2). The index f is used to outline the faulty case. Note that $\psi_i = 1$ indicates that the ith FEEP thruster is closing itself. The case of the ith thruster blocking itself when in operation corresponds to

$$\psi_i(t) = 1 - \frac{c}{u_{\text{FEEP}_i}(t)}$$

where c is a constant value.

Then, substituting C_p in Eq. (21) by $(I_{12} - \psi)$ and using an approximation of the fault model in terms of an additive fault type one, it follows from Eqs. (21–23) that

$$\begin{cases} \dot{x} = f(x, \varpi_{\text{spin}}) + E_1 h(\varpi_\alpha, \varpi_{\text{spin}}) + BMC_P x_P + \sum_{i=1}^{12} K_{1_i} f_i \\ \dot{x}_P = A_P x_P + B_P T \\ \dot{y} = g(x) + E_2 h(\varpi_\alpha, \varpi_{\text{spin}}) + DMC_P x_P + \sum_{i=1}^{12} K_{2_i} f_i \end{cases} \tag{25}$$

$$y_i = e^{-\rho_i s}\bar{y}_i + n_i \tag{26}$$

$$T = M^+ \begin{pmatrix} K_\Theta(s)\hat{\Theta} \\ K_\Gamma(s)\hat{\Gamma} \end{pmatrix} \tag{27}$$

where (K_{1_i}, K_{2_i}) is the ith fault signature associated with the ith fault mode f_i. This approximation makes sense as long as the Microscope control law keeps stability in faulty situations. The interested reader can refer to Isermann [5] and Frank et al. [46] for a discussion of such an approximation.

Finally, noting that Microscope is controlled around the equilibrium point $\Theta = 0$, $\Gamma = 0$, $\varpi_\alpha = \text{constant}$, and $\varpi_{\text{spin}} = \text{constant}$, one can derive from Eqs. (25–27) a linear model by means of a first-order approximation of the nonlinear equations around the equilibrium point. For the time delays ρ_i, a first-order Padé approximation is used. This boils down to the linear time-invariant (LTI) model:

$$y = P(s) \begin{pmatrix} f_i \\ h(\varpi_\alpha, \varpi_{\text{spin}}) \\ u \end{pmatrix} + n, \qquad i = 1, \ldots, 12 \tag{28}$$

$$u = M^+ \begin{pmatrix} K_\Theta(s)\hat{\Theta} \\ K_\Gamma(s)\hat{\Gamma} \end{pmatrix} \tag{29}$$

which is also suitable for the H_∞/H_- FDI filters design method proposed in Henry and Zolghadri [22,23]. In this formulation, we assume that all considered faults f_i, $i = 1, \ldots, 12$ are detectable (see Massoumia [47] for more details on fault detectability).

To validate the LTI model equations (28) and (29), linear vs nonlinear simulations were performed. The simulation scenario corresponds to a constant disturbance applied at $t = 0$ s. A fault is simulated in the first FEEP thruster at $t = 150$ s. Our goal was to validate the transient behavior and the steady state of the output

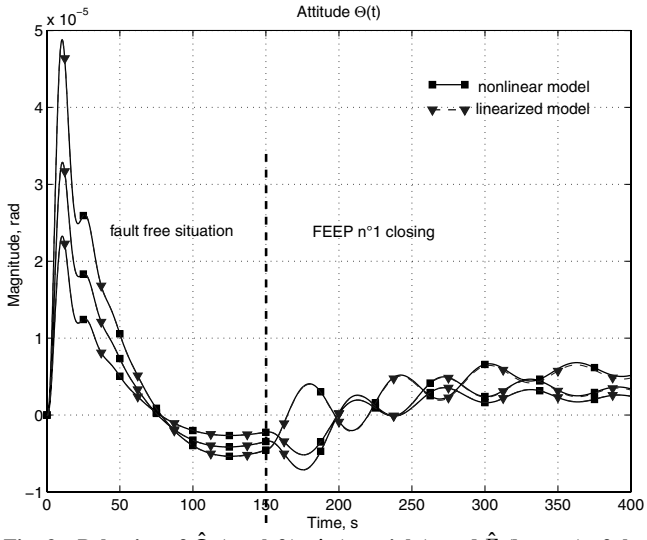

Fig. 3 Behavior of $\hat{\Theta}$ (top left), $\dot{\varpi}$ (top right), and $\hat{\Gamma}$ (bottom) of the linearized model (triangle) vs the nonlinear model (square).

signals $\hat{\Theta}(t)$, $\dot{\varpi}(t)$, and $\hat{\Gamma}(t)$ predicted by the linearized model in both fault free and faulty situations. To allow a better comparison, the simulations are performed without the measurement noises. Figure 3 illustrates the behavior of $\hat{\Theta}(t)$ predicted by both the linearized model (plots with triangles) and the nonlinear model (plots with squares). For brevity, the plots of $\dot{\varpi}(t)$ and $\hat{\Gamma}(t)$ are not presented. As it can be seen, the linear model equations (28) and (29) successfully approximate the nonlinear model.

III. Design of the FDI Schemes

In this section, two FDI schemes able to detect and isolate thruster faults despite the presence of the disturbances $h(\varpi_\alpha, \varpi_{\text{spin}})$ and the noises n are considered within the H_∞/H_- setting.

The first FDI scheme consists of a bank of 12 residual generators that are designed so that the sensitivity level of the ith residual with respect to the ith FEEP thruster fault f_i is maximized in the H_--norm sense, while guaranteeing robustness against n and $h(\varpi_\alpha, \varpi_{\text{spin}})$ in the H_∞-norm sense. An original aspect in the proposed scheme is that the a priori knowledge of $h(\varpi_\alpha, \varpi_{\text{spin}})$ given by Eqs. (7–20) are used to, say, pilot the 12 residual generators. This allows for the enhancement of the robustness level of the FDI scheme against $h(\varpi_\alpha, \varpi_{\text{spin}})$.

Next, the residuals are postprocessed by a fault isolation stage to isolate the specific fault. The proposed method is based on the evaluation of a cross-correlation criterion between the residuals and the signature that a given FEEP fault has on the controlled thruster open rate T_i, $i = 1, \ldots, 12$.

The second FDI strategy is also based on a bank of 12 H_∞/H_- residual generators. The filters are designed so that the ith residual is made sensitive to f_i in the H_--norm sense, while being robust against the set of the 11 remaining faults in the H_∞-norm sense (in the following, this set will be denoted as $\bar{f}$).

The major difference with the first FDI strategy is that the robustness requirements against n and $h(\varpi_\alpha, \varpi_{\text{spin}})$ are not formulated within the H_∞/H_- design procedure. These are achieved by incorporating a band-stop and a low-pass component into the residual generators.

A. Design of the First FDI Strategy

The proposed FDI scheme is illustrated in Fig. 4. As mentioned, it uses $h(\varpi_\alpha, \varpi_{\text{spin}})$ predicted by the mathematical models of C_m, C_g, C_{aero}, C_{solar}, F_{aero}, and F_{solar} given by Eqs. (7–20) as an input to the 12 residual generators. Note that we use the controlled moments and forces $\bar{u} = (\bar{C}^T \bar{F}^T)^T = \begin{pmatrix} K_\Theta(s)\hat{\Theta} \\ K_\Gamma(s)\hat{\Gamma} \end{pmatrix}$ for the residual generators rather than the controlled open rates T_i, $=1, \ldots, 12$ of the thrusters.

1. *Design of the 12 H_∞/H_- Residual Generators*

In the interest of brevity, throughout this section an earnest attempt will be made to avoid duplicating materials presented in Henry and Zolghadri [22,23]. Thus, in the following we suppose that the reader is familiar with the developments given in Henry and Zolghadri [22,23], and we will refer the reader to these papers for necessary proofs.

Let us consider the problem of the design of the ith H_∞/H_- residual generator (this problem is illustrated in Fig. 5a). Let the ith residual signal r_i be given by

$$r_i = z_i - \hat{z}_i \tag{30}$$

where $\hat{z}_i$ is an estimation of $z_i = M_{y_i} y + M_{u_i} u$, a subset of measurements y and inputs u. $M_{y_i} \in \mathbb{R}^{1\times 9}$ and $M_{u_i} \in \mathbb{R}^{1\times 12}$ are the two (constant) residual structuring matrices. For clarity, the subscript i is ignored from now on.

Using some linear fractional algebra manipulations, the setup depicted in Fig. 5a can be recast according to the setup illustrated in Fig. 5b, in which the augmented disturbances vector d is defined according to $d = (h^T(\varpi_\alpha, \varpi_{\text{spin}})n^T)^T$ and in which $\bar{P}(s, M_y, M_u)$ is deduced from $P(s)$, $K_\Theta(s)$, $K_\Gamma(s)$, M_y, and M_u. And so the problem turns out to be the design of M_y, M_u, and $L(s)$:$\hat{z} = L(s)\binom{y}{u}$ such that 1) (S.1): $\|T_{d\to r}\|_\infty < \gamma_1$ where $T_{d\to r}$ denotes the closed-loop transfer between r and d; and 2) (S.2): $\|T_{f\to r}\|_- > \gamma_2$ over a specified frequency range Ω where $T_{f\to r}$ denotes the closed-loop transfer between r and f and Ω is the frequency range in which (S.2) is required to yield.

In this formulation, $\|\mathbf{M}\|_\infty = \sup_\omega \bar{\sigma}(\mathbf{M}(j\omega))$ is the H_∞ norm of $\mathbf{M}$ and $\bar{\sigma}(\bullet)$ denotes the maximum singular value. $\|\mathbf{M}\|_- = \inf_{\omega\in\Omega} \underline{\sigma}(\mathbf{M}(j\omega))$, $\Omega = [\omega_1; \omega_2]$ denotes the H_- norm of $\mathbf{M}$ introduced in Chen and Patton [1] and Ding et al. [35]. $\underline{\sigma}(\mathbf{M}(j\omega))$

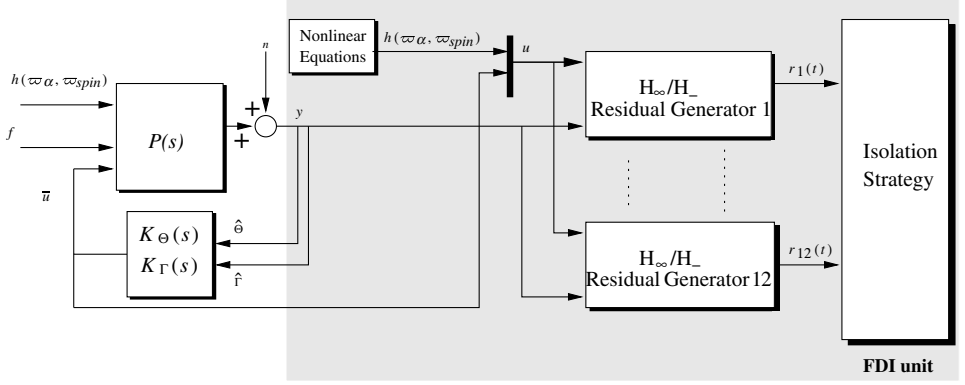

Fig. 4 FDI scheme.

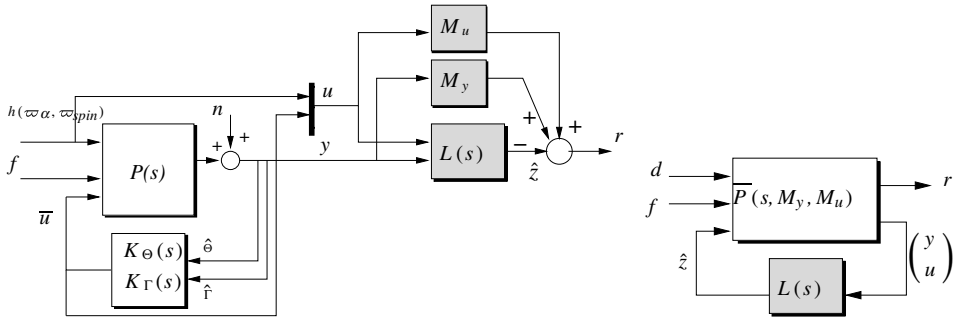

Fig. 5 H_∞/H_- fault detector design problem.

denotes the minimum nonzero singular value of the matrix $\mathbf{M}(j\omega)$ and $\Omega = [\omega_1; \omega_2]$ the evaluated frequency range in which $\underline{\sigma}(\mathbf{M}(j\omega)) \neq 0$.

The specification (S.1) represents the worst-case robustness of the residual to spatial disturbances $h(\varpi_\alpha, \varpi_{\text{spin}})$ and noises n, and the specification (S.2) is the fault sensitivity objective allowing to guarantee a high detection performance level of the detection scheme. Of course, the smaller γ_1 and the bigger γ_2 are, the better the fault detection performances will be.

Following the method proposed in Henry and Zolghadri [22,23], the requirements (S.1) and (S.2) are expressed in terms of loop shapes, that is, of desired gain responses for the appropriate closed-loop transfers. These shaping objectives are then turned into uniform bounds by means of the shaping filters.

To proceed, let W_d and W_f denote the (dynamical) shaping filters associated with (S.1) and (S.2), respectively. Because of the definition of d, it is natural to choose W_d according to $W_d = \text{diag}(W_h, W_n)$. W_h allows for the specification of robustness requirements against the disturbances $h(\varpi_\alpha, \varpi_{\text{spin}})$, and W_n allows for the formulation of robustness objectives against n. Following Eqs. (7–20), it appears that the spatial disturbances $h(\varpi_\alpha, \varpi_{\text{spin}})$ manifest themselves at the frequency ranges ω_α and $\omega_\alpha - \omega_{\text{spin}}$. Then, it is desired to have a rejecting behavior of $T_{h(\varpi_\alpha, \varpi_{\text{spin}})\to r}(j\omega)$ at those frequencies. $T_{h(\varpi_\alpha, \varpi_{\text{spin}})\to r}(j\omega)$ denotes the components of $T_{d\to r}(j\omega)$ associated with $h(\varpi_\alpha, \varpi_{\text{spin}})$. This leads to the choice of W_h as a band-stop filter centered to $\omega_c = \frac{2\omega_\alpha - \omega_{\text{spin}}}{2}$ with side band ξ chosen to cover the frequency range $[\omega_\alpha - \omega_{\text{spin}}; \omega_\alpha]$ rd/s, that is,

$$W_h = \gamma_h \frac{1 + \frac{2\xi}{\omega_c} s + \frac{1}{\omega_c^2} s^2}{\frac{2\xi}{\omega_c} s(1 + \tau_h s)} I_6 \tag{31}$$

The positive constant γ_h is introduced to manage the gain of W_h. This allows for the management of the robustness level of the fault detection scheme against the spatial disturbances $h(\varpi_\alpha, \varpi_{\text{spin}})$ (see Henry and Zolghadri [22,23,40] if necessary). The parameter τ_h is introduced to make W_h invertible (see later, Lemma 1).

With regard to W_n, because $y = (\hat{\Theta}^T \dot{\omega}^T \hat{\Gamma}^T)^T$, it is natural to fix W_n according to $W_n = \text{diag}(W_{n\Theta} I_3, W_{n\dot{\omega}} I_3, W_{n\hat{\Gamma}} I_3)$ where $W_{n\Theta}$, $W_{n\dot{\omega}}$, and $W_{n\hat{\Gamma}}$ are referred to $\hat{\Theta}$, $\dot{\omega}$, and $\hat{\Gamma}$, respectively. Coming back to the discussion on modeling the navigation unit presented in Sec. II.B, it is natural to define $W_{n\dot{\omega}}^{-1}$ and $W_{n\hat{\Gamma}}^{-1}$ equal to the coloring filters used to model n. As a consequence, the components of $W_{n\dot{\omega}}^{-1}$ and $W_{n\hat{\Gamma}}^{-1}$ referred to the x axes are high-pass filters of an order 6 and those referred to the y and z axes are high-pass filters of a second order. In fact, to reduce the computation time and the order of the fault detection filters, $W_{n\dot{\omega}}^{-1}$ and $W_{n\hat{\Gamma}}^{-1}$ are chosen to be equal and as an upper bound of the coloring filters, so that they involve less poles/zeros. This boils down to the following definition for $W_{n\dot{\omega}} = W_{n\hat{\Gamma}}$

$$W_{n\dot{\omega}} = W_{n\hat{\Gamma}} = \gamma_{\text{acc}} \frac{(1 + \tau_1 s)^2}{(1 + \tau_2 s)^2} \qquad \tau_1 = 0.2 \text{ s}, \qquad \tau_2 = 10 \text{ s} \tag{32}$$

The positive constant γ_{acc} is introduced to manage the gain of $W_{n\dot{\omega}} = W_{n\hat{\Gamma}}$. Clearly, $W_{n\dot{\omega}}$ and $W_{n\hat{\Gamma}}$ are low-pass filters (remember that $W_{n\dot{\omega}}^{-1}$ and $W_{n\hat{\Gamma}}^{-1}$ are high-pass filters). In other words, a high frequency attenuation of $T_{n_{\dot{\varpi}\Gamma}\to r}(j\omega)$ is required at those frequencies at which the energy content of n is likely concentrated, that is, at $\omega \geq 5$ rad/s. In this formulation, $T_{n_{\dot{\varpi}\Gamma}\to r}(j\omega)$ denotes the components of $T_{d\to r}(j\omega)$ referred to $\dot{\varpi}$ and $\hat{\Gamma}$.

Similarly, $W_{n\Theta}$ is chosen as a constant γ_{att} because, for $\hat{\Theta}$, we assumed a Gaussian white noise (see Sec. II.B).

For the purpose of the fault sensitivity objectives, we consider that the faults we are interested in manifest themselves in low frequencies. This boils down to a first-order low-pass filter for W_f with a cutting frequency ω_f, that is,

$$W_f = \gamma_2 \frac{1}{1 + \tau_f s} \qquad \tau_f = \frac{1}{\omega_f} \tag{33}$$

The solution is then handled using the following lemma:

Lemma 1: Consider the shaping filters W_d and W_f as already defined. We assume that W_d and W_f have been scaled such that $\|W_d\|_\infty \leq \gamma_1$ and $\|W_f\|_- \geq \gamma_2$. Then, (S.1) yields if and only if

$$\|T_{d\to r} W_d^{-1}\|_\infty < 1 \tag{34}$$

Now, introduce W_F, a right invertible transfer matrix so that $\|W_f\|_- = \frac{\gamma_2}{\lambda}\|W_F\|_-$ and $\|W_F\|_- > \lambda$, where $\lambda = 1 + \gamma_2$. Define the signal $\tilde{r}$ such that $\tilde{r} = r - W_F(s) f$. Then a sufficient condition for the fault sensitivity specification (S.2) to hold is

$$\|T_{f\to\tilde{r}}\|_\infty < 1 \tag{35}$$

where $T_{f\to\tilde{r}}$ denotes the closed-loop transfer between $\tilde{r}$ and f. □

Using the above lemma, the H_∞/H_- residual generator design problem can be formulated in a fictitious H_∞ framework: combining Eqs. (34) and (35) into a single H_∞ constraint and including γ_1, λ, W_F, and the shaping filter W_d into the model P leads to a new model $\tilde{P}(s, M_y, M_u)$ depending on the residual structuring matrices M_y and M_u so that

$$\begin{pmatrix} r \\ \tilde{r} \end{pmatrix} = \mathcal{F}_l(\tilde{P}(s, M_y, M_u), L(s))\mathbf{d} \tag{36}$$

where $\mathcal{F}_l(\tilde{P}(s, M_y, M_u), L(s))$ denotes the lower linear fractional representation of $\tilde{P}(M_y, M_u, s)$ by $L(s)$. $\mathbf{d}$ is defined according to $\mathbf{d} = (\tilde{d}^T \quad f)^T$ where $\tilde{d}$ is a fictitious signal generating d through W_d.

Then, a sufficient condition for specifications (S.1) and (S.2) to hold is

$$\|\mathcal{F}_l(\tilde{P}(M_y, M_u), L)\|_\infty < 1 \tag{37}$$

This equation seems to be similar to a standard H_∞ one. In fact, this is not the case because the transfer $\tilde{P}(M_y, M_u)$ depends on M_y and M_u that are unknown. The following proposition allows us to overcome

this problem. A complete proof can be found in Henry and Zolghadri [22]:

Proposition 1: We assume that $\tilde{P}(M_y, M_u)$ admits the following general state-space equations:

$$\tilde{P}:\begin{cases}\dot{x} = Ax + B_1\mathbf{d} + B_2\hat{z}\\ (r^T\tilde{r}^T)^T = C_1(M_y, M_u)x + D_{11}(M_y, M_u)\mathbf{d} + D_{12}\hat{z}\\ (y^T u^T)^T = C_2 x + D_{21}\mathbf{d} + D_{22}\hat{z}\end{cases} \tag{38}$$

where A, B_1, B_2, $C_1(M_y, M_u)$, C_2, $D_{11}(M_y, M_u)$, D_{12}, D_{21}, and D_{22} are matrices of adequate dimensions. Let $\mathcal{W} = (\,C_2 \quad D_{21}\,)^{\perp}$. Then there exists a solution of Eq. (37) if and only if there exist $\gamma < 1$, M_y, M_u, and two symmetric matrices R, S solving the following semidefinite programming (SDP) problem:

$$\text{minimize } \gamma \text{ subject to } \begin{pmatrix} AR + RA^T & B_1\\ B_1^T & -\gamma I\end{pmatrix} < 0$$

$$\begin{pmatrix}\mathcal{W} & 0\\ 0 & I\end{pmatrix}^T \begin{pmatrix} A^TS + SA & SB_1 & C_1^T(M_y, M_u)\\ B_1^TS & -\gamma I & D_{11}^T(M_y, M_u)\\ C_1(M_y, M_u) & D_{11}(M_y, M_u) & -\gamma I\end{pmatrix} \times \begin{pmatrix}\mathcal{W} & 0\\ 0 & I\end{pmatrix} < 0 \qquad \begin{pmatrix} R & I\\ I & S\end{pmatrix} \geq 0 \tag{39}$$

The state-space matrices of the dynamical filter $L(s)$ are then computed from the unique solution (R, S, γ) (see Henry and Zolghadri [22] for a computational procedure). □

Because Lemma 1 involves a sufficient condition and because the combination of Eqs. (34) and (35) into Eq. (37) brings conservativeness into the design, $\gamma \geq 1$ does not imply with certainty that the computed solution does not satisfy the required objectives. Thus, as a postdesign analysis procedure, the principal gains of the shaping filters can be plotted vs the gain responses of the appropriate closed-loop transfers (seen later).

2. *Computational Results*

The 12 detection filters are computed following Lemma 1 and Proposition 1. The SDPT3 solver is used to perform the optimization problem equation (39). For each synthesis, the numerical values of γ_{acc}, γ_{att}, and γ_h have been fixed to 10^{-2}, 0.1, and 3.10^{-5}, respectively. Note that these small values indicate a high robustness level of the residual generators against n and $h(\varpi_\alpha, \varpi_{\text{spin}})$ because they indicate the attenuation level of $h(\varpi_\alpha, \varpi_{\text{spin}})$ and n on $r_i(t)$, $i = 1, \ldots, 12$. Furthermore the numerical values of γ_2 and ω_f are maximized in each case. This allows for the achievement of high sensitivity performances of the detection filters. Figure 6 illustrates the principal gains of the residual generator 1. For brevity, the other fault detection filters are not considered.

To analyze the computed residual generators, the principal gains $\bar{\sigma}(T_{d\to r}^k(j\omega))$ and $\underline{\sigma}(T_{f\to r}(j\omega))$ are plotted vs the objectives W_d^k and W_f. The notation k is introduced to underline that the analysis is

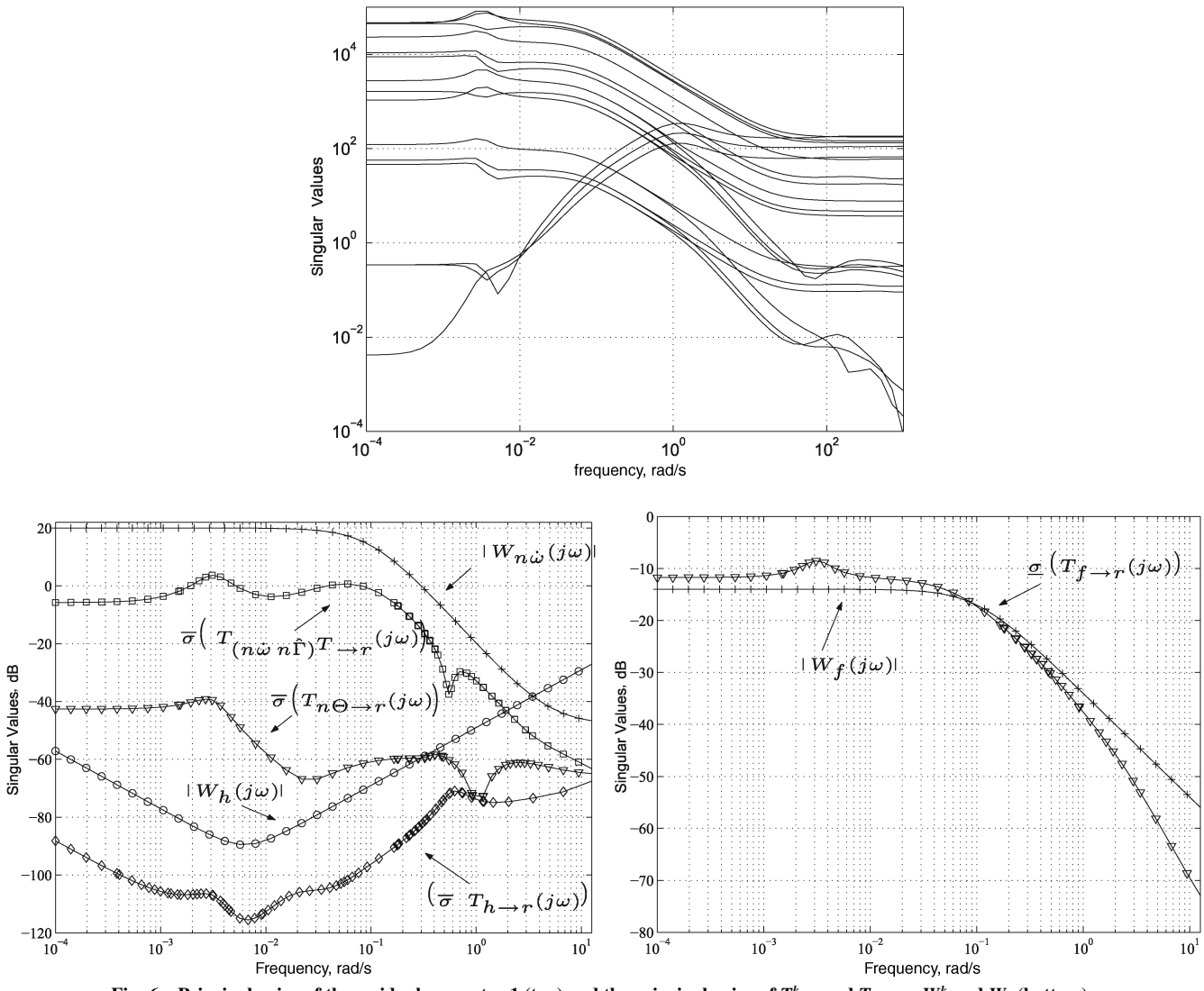

Fig. 6 Principal gains of the residual generator 1 (top) and the principal gains of $T_{d\to r}^k$ and $T_{f\to r}$ vs W_d^k and W_f (bottom).

performed with respect to $h(\varpi_\alpha, \varpi_{\text{spin}})$ and each component of n. Figure 6 illustrates the plots for the residual generator 1 case. As can be seen in the figure, $\bar{\sigma}(T^k_{d\to r}(j\omega)) < |W^k_d(j\omega)|, \ \forall\ \omega$ and $\underline{\sigma}(T_{f\to r}(j\omega)) > |W_f(j\omega)|, \forall\ \omega \in \Omega \approx [0; 0.1]$ rad/s, which indicate that the requirements (S.1) and (S.2) are fulfilled. Furthermore, the small gap between $\bar{\sigma}(T^k_{d\to r}(j\omega))$ and $|W^k_d(j\omega)|, \forall\ \omega$ and between $\underline{\sigma}(T_{f\to r}(j\omega))$ and $|W_f(j\omega)|, \ \forall\ \omega \in \Omega$ illustrate a not-too-conservative solution.

3. Isolation Strategy

After a judgement "fault," fault isolation is required because one desires to gain deeper insight into the faulty situation. The aim is to identify which FEEP thruster became damaged. The proposed isolation strategy is based on the following cross-correlation criterion between the residuals r_i and the associated controlled thruster open rate T_i:

$$\varrho_i(\tau) = \left| \frac{1}{N} \sum_{k=\tau}^{\tau+N} (r_i(k) - \bar{r}_i)(T_i(k) - \bar{T}_i) \right|, \qquad i = 1, \ldots, 12 \quad (40)$$

$\bar{r}_i$ and $\bar{T}_i$ denote the mean values of $r_i(k)$, $k = \tau, \ldots, \tau + N$ and $T_i(k)$, $k = \tau, \ldots, \tau + N$, respectively. The isolation procedure works in such a way that when $\varrho_K(\tau)$ is higher or equal to a prescribed value ρ, then the fault is declared to be localized in the Kth actuator. For real-time reason, this criterion is computed on a N-length sliding window. It should be pointed out that such an isolation strategy

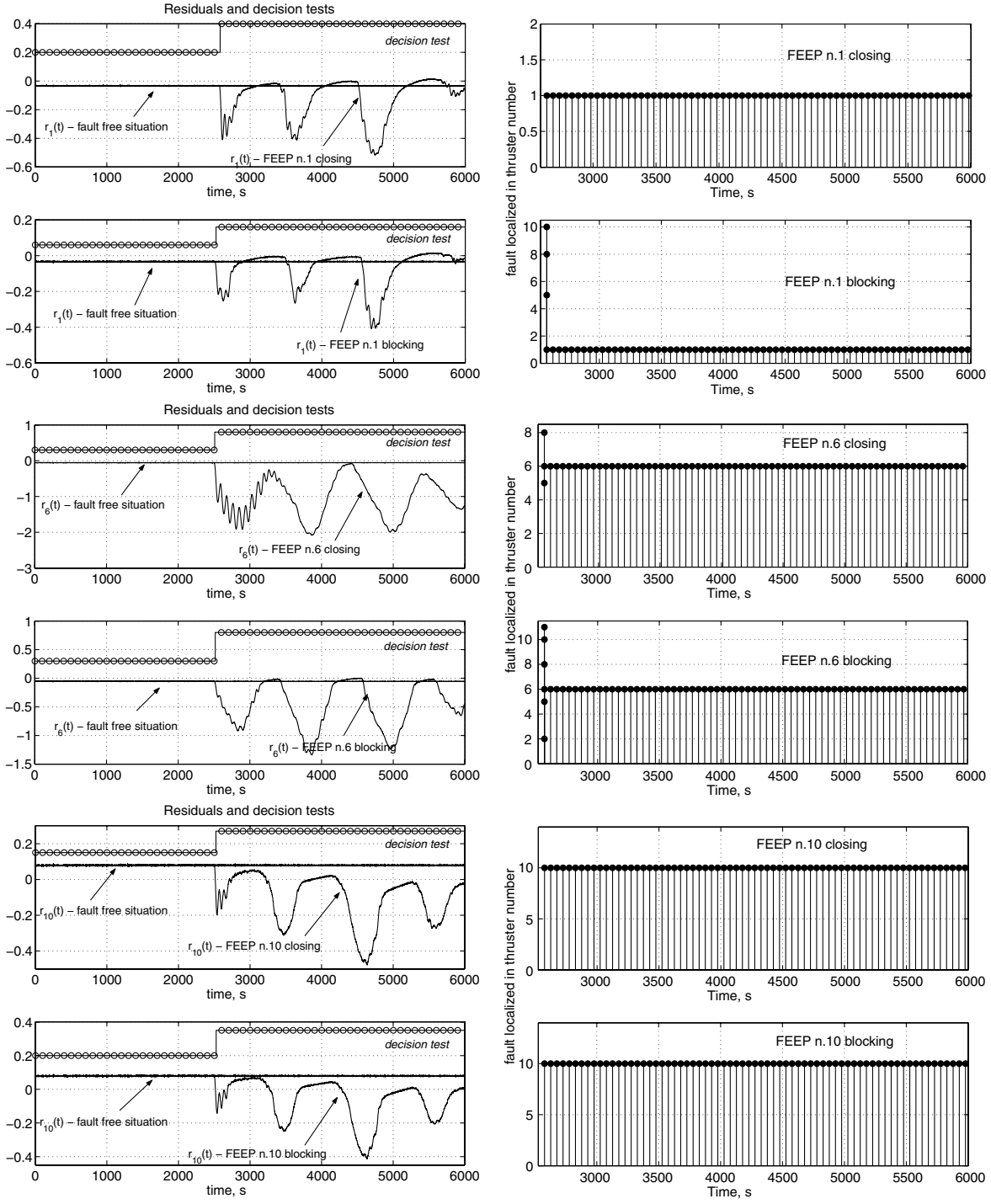

Fig. 7 Behavior of the residuals in fault free and faulty situations + the decision test (left) and the isolation criteria $\varrho(\tau)$ (right).

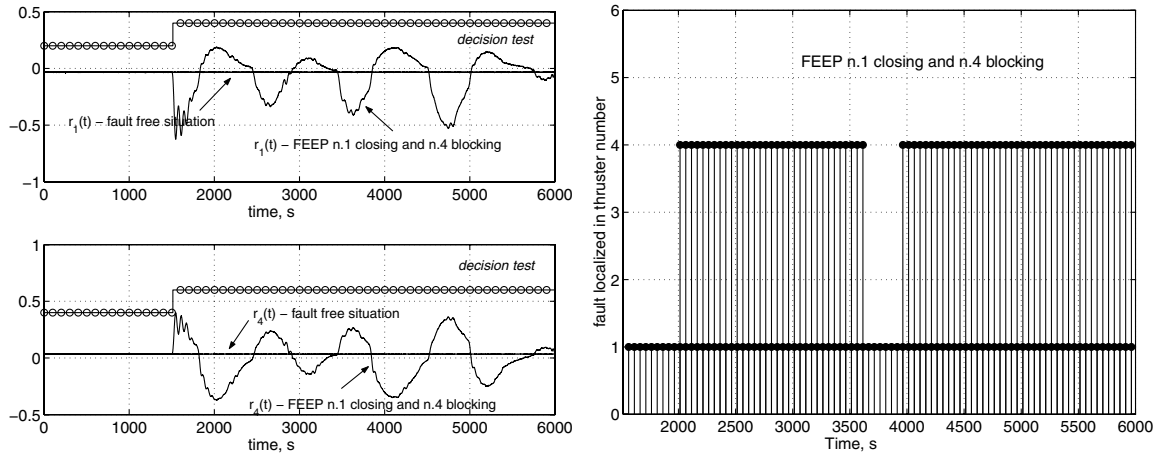

Fig. 8 Behavior of the residuals in fault free and faulty situations and the decision test (left) and the isolation criteria $\varrho(\tau)$ (right). Thruster 1 closing and thruster 4 blocking.

makes sense because the sensitivity of the ith residual with respect to the ith FEEP thruster fault has been maximized in the H_--norm sense.

4. *Nonlinear Simulation Results*

The 12 detection filters are converted to discrete time using a Tustin approximation and implemented within the nonlinear simulator of Microscope. The simulations have been performed on an orbital period, that is, $t = 0 \ldots 6000$ s. To make a final decision about the fault, a sequential Wald decision test applied to $\|r(t)\|_2$ is implemented within the simulator. The probabilities of nondetection and false alarms have been fixed to 0.1%. The isolation strategy is also implemented within the nonlinear simulator of Microscope. Figure 7 illustrates the behavior of the residuals $r_i(t)$, $i = 1, \ldots, 12$ and the behavior of the decision test and the isolation criteria $\varrho(\tau)$ for some faulty situations. As can be seen in the figure, after a small transient behavior, all faults are successfully detected and isolated by the FDI unit.

Finally, the case of multiple faults is considered. The simulated scenario corresponds to the first FEEP thruster closing itself at the same time as the fourth blocks itself. Figure 8 illustrates the behavior of the residuals $r_1(t)$ and $r_4(t)$ and the decision test. The behavior of the isolation criteria $\varrho(\tau)$ is also illustrated in the figure. As can be seen, the two faults are successfully detected and "quite well" isolated.

Remark 1: We have performed a lot of simulations to evaluate the performances of the proposed FDI scheme. In each case, the faults were successfully detected. However, the isolation strategy failed to isolate the faults in some cases (see Fig. 9, in which an example is given). Fortunately, such problems have been rarely observed and manifest themselves during a transient time.

B. Design of the Second FDI Strategy

We shall begin this section by coming back to Remark 1. Nonlinear simulations have revealed that there exists an unacceptable transient behavior of the fault isolation criteria $\varrho(\tau)$ in some cases. A solution to this problem may consist of increasing the numerical values of N and/or ρ, but this solution is very time and memory consuming. On the other hand, the proposed FDI strategy involves the use of 12 residual generators that appear to be of order 53/54. Such a complex FDI scheme is also time and memory consuming, even if the filters are converted to discrete time. As a solution to this problem, a gramian-based balanced reduction procedure was performed. Unfortunately, the FDI strategy obtained by this method led to many false alarms and was therefore judged unsatisfactory.

As an alternative, the following FDI procedure is proposed. First, remember that the energy content of $h(\varpi_\alpha, \varpi_{\text{spin}})$ is located in the frequency ranges ϖ_α and $\varpi_\alpha - \varpi_{\text{spin}}$. Because we assume that the energy content of the faults we are interested in is located in a frequency range $\Omega{:}[\varpi_\alpha - \varpi_{\text{spin}}, \varpi_\alpha] \cap \Omega = \emptyset$, the robustness objectives against $h(\varpi_\alpha, \varpi_{\text{spin}})$ can be achieved by including a band-stop component into the residual generators at $[\varpi_\alpha - \varpi_{\text{spin}}, \varpi_\alpha]$. Similarly, because the energy content of n is likely concentrated in the frequency range $\Omega_n \approx [0.1; 10]$ rad/s so that $\Omega_n \cap \Omega = \emptyset$, the robustness objectives against n can be achieved by including a simple low-pass component into the residual generators.

Then, the problem turns out to be the design of 12 H_∞/H_- filters in the general form given by Eq. (1) so that the ith residual is made sensitive (in the H_--norm sense) against the ith FEEP thruster fault f_i, while remaining robust (in the H_∞-norm sense) against the remaining 11 faults $\bar{f}$. The robustness objectives against $h(\varpi_\alpha, \varpi_{\text{spin}})$ and n are obviously achieved by the rejecting and the low-pass components of the residual generators. Note that this technique is well known in the robust control community in which a controller can be composed by an integral-based fixed part and another part that is designed using H_∞/μ techniques. Here, the fixed part is nothing other than the band-stop and the low-pass components, and the design part consists of $L_i(s)$, M_{y_i}, and M_{u_i}, $i = 1, \ldots, 12$ [see Eq. (1)].

1. *Design of $L_i(s)$, M_{y_i}, and M_{u_i}, $i = 1, \ldots, 12$*

The problem to be solved consists now in the design of M_{y_i}, M_{u_i}, and $L_i(s){:}\hat{z}_i = L_i(s)\binom{y_j}{T_i}$, $j = 4, \ldots, 9$ that define the 12 residuals:

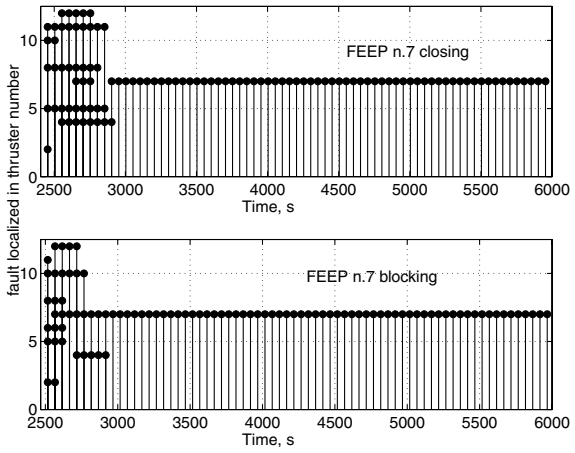

Fig. 9 Behavior of the isolation criteria $\varrho(\tau)$. Thruster 7 closing (top) and blocking (bottom).

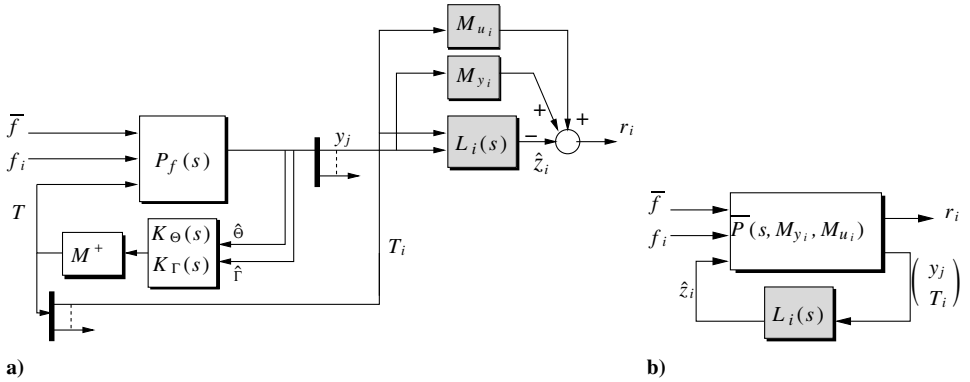

Fig. 10 H_∞/H_- fault detector design problem.

$$r_i = M_{y_i} y_j + M_{u_i} T_i - L_i(s)\begin{pmatrix} y_j \\ T_i \end{pmatrix} \qquad \begin{matrix} i = 1, \ldots, 12 \\ j = 4, \ldots, 9 \end{matrix} \tag{41}$$

such that (see Fig. 10a) 1) (S.1): $\|T_{\bar{f}\to r_i}\|_\infty < \gamma_1$ where $T_{\bar{f}\to r_i}$ denotes the closed-loop transfer between r_i and $\bar{f}$, and 2) (S.2): $\|T_{f_i\to r_i}\|_- > \gamma_2$ over the specified frequency range Ω where $T_{f_i\to r_i}$ denotes the closed-loop transfer between r_i and f_i.

In this formulation, we use the last six components of the output vector y, that is, the angular and linear accelerations $\dot{\varpi}$ and $\hat{\Gamma}$, and the ith thruster open rate T_i, that is, the ith component of T, to derive the ith residual signal r_i, y, and T as defined according to Eqs. (28) and (29). This particular choice of the input/output subset has been revealed to lead to high FDI performances.

Because of the definitions of $\bar{f}$ and f_i, the specification (S.1) represents the fault isolation objective, and the specification (S.2) is the fault sensitivity requirement allowing the guarantee of a high detection performance level of the detection scheme.

Following the method proposed in Henry and Zolghadri [22,23], the requirements (S.1) and (S.2) are expressed in terms of desired gain responses for the appropriate closed-loop transfers. These

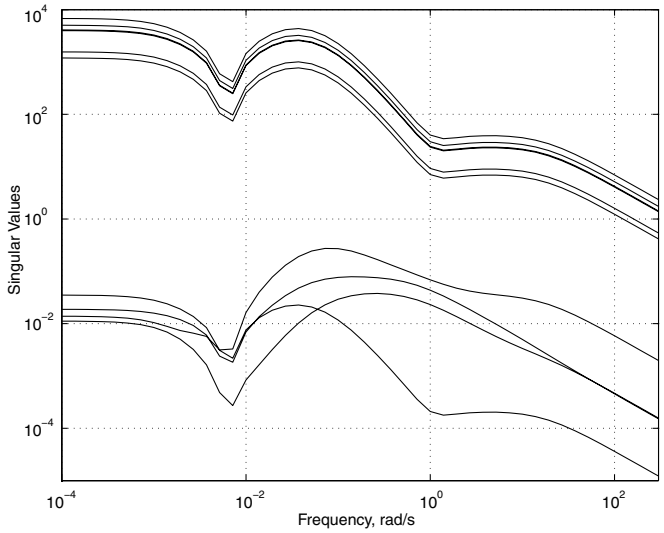

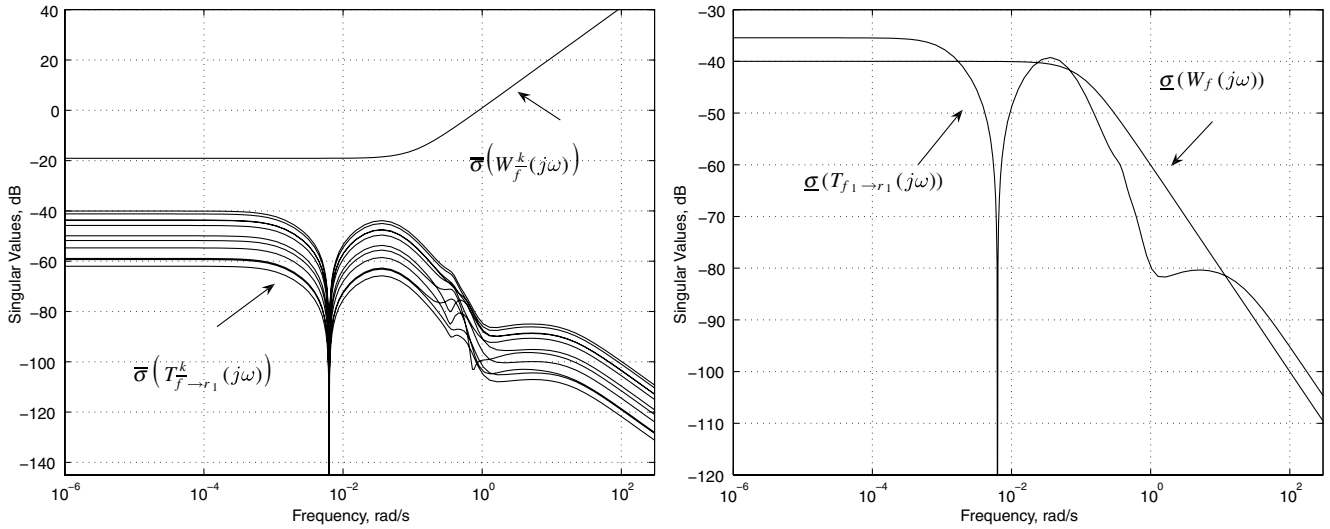

Fig. 11 Principal gains of the residual generator 1 (top) and the principal gains of $T_{\bar{f}\to r_1}^k$ and $T_{f_1\to r_1}$ vs $W_{\bar{f}}^k$ and W_f (bottom).

shaping objectives are then turned into uniform bounds by means of the shaping filters. To proceed, let $W_{\bar{f}}$ and W_f denote the (dynamical) shaping filters associated with (S.1) and (S.2), respectively. Following Sec. III.A, W_f is chosen as a first-order low-pass filter with a cutting frequency ω_f [see Eq. (33)]. For the purpose of the isolation objectives, due to the definition of $\bar{f}$, it is natural to choose $W_{\bar{f}}$ according to

$$W_{\bar{f}}(s) = \mathrm{diag}(\ldots \gamma_{f_i} \ldots) W_f^{-1}(s), \qquad i = 1, \ldots, 11 \tag{42}$$

where γ_{f_i}, $i = 1, \ldots, 11$ are (positive) constants introduced to manage the gain of each component of $W_{\bar{f}}$. This allows the management of the isolation performances of a given residual generator (see Henry and Zolghadri [22,23,40] if necessary).

The H_∞/H_- filter design problem is then recast in a fictitious H_∞ framework using Lemma 1 (see Fig. 10b for easy reference), and M_{y_i}, M_{u_i}, and the state-space matrices of the dynamical filters $L_i(s)$ are computed using Proposition 1.

2. *Computational Results*

Similar to the first proposed FDI strategy, the numerical values of γ_2 and ω_f are maximized. This allows for the achievement of high sensitivity performances of the fault detection filters. The SDPT3 solver is used to perform the optimization problem equation (39). To reduce the complexity of the FDI scheme, a gramian-based balanced reduction procedure is applied to each filter. The reduced filters are found to be of an order between 7 and 10 instead of 26 for the original ones. Figure 11 illustrates the principal gains of the residual generator 1. For brevity, the other fault detection filters are not considered.

To analyze the computed solutions, the principal gains $\bar{\sigma}(T^k_{\bar{f}\to r_i}(j\omega))$ and $\underline{\sigma}(T_{f\to r_i}(j\omega))$ are plotted vs the objectives $W^k_{\bar{f}}$ and W_f. The notation k is introduced to underline that the analysis is performed with respect to each component of $\bar{f}$. Figure 11 illustrates the plots for the residual generator 1 case. As can be seen, $\bar{\sigma}(T^k_{\bar{f}\to r_1}(j\omega)) < \bar{\sigma}(W^k_{\bar{f}}(j\omega))\forall\ \omega$ and $\underline{\sigma}(T_{f_1\to r_1}(j\omega)) > \underline{\sigma}(W_f(j\omega))\forall\ \omega \in \Omega \approx [0; 10^{-3}]$ rad/s, which indicate that the requirements (S.1) and (S.2) are fulfilled. Note that the effects of the (a priori fixed) band-stop and low-pass components of the residual generators appear clearly.

3. *Nonlinear Simulation Results*

The 12 detection filters are next converted to discrete time using a Tustin approximation and implemented within the nonlinear simulator of Microscope. Figure 12 illustrates the behavior of the residuals $r_i(t)$, $i = 1, \ldots, 12$ for some faulty situations. To make a final decision about the fault, a sequential Wald decision test applied to $\|r(t)\|_2$ is also implemented within the simulator. The probabilities of nondetection and false alarms have been fixed to 0.1%. As can be seen in the figures, all faults are successfully detected and isolated by the FDI unit.

Finally, the case of multiple faults is considered. The simulated scenario corresponds to the first FEEP thruster closing itself at the same time as the fourth blocks itself. Figure 13 illustrates the

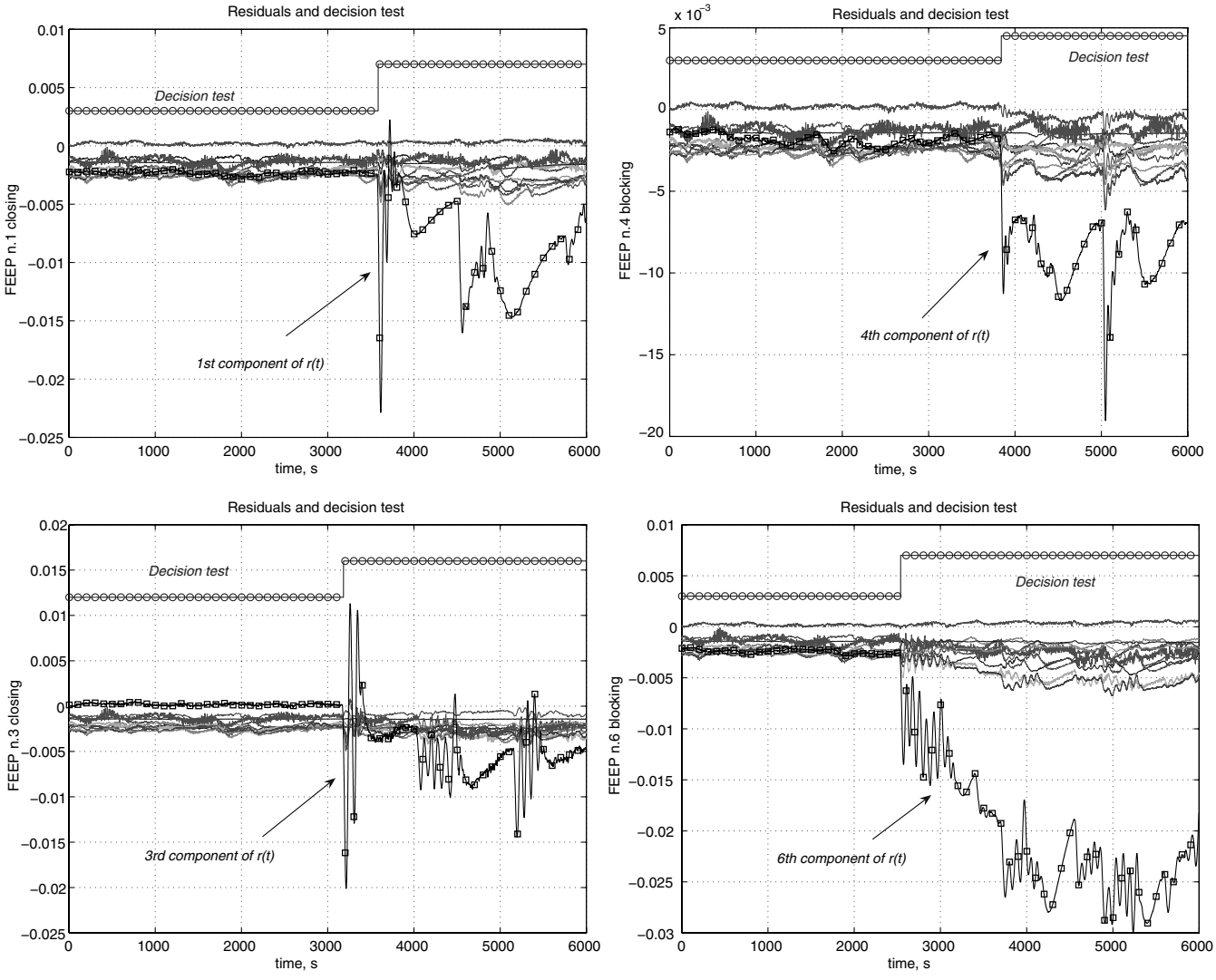

Fig. 12 Behavior of the residuals and the decision test.

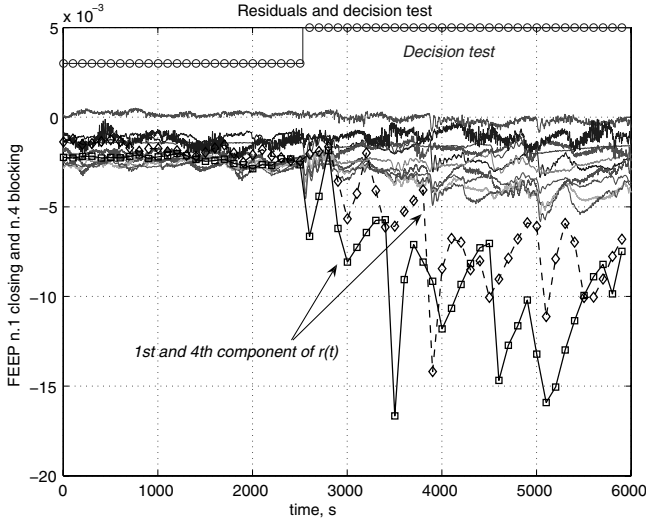

Fig. 13 Thruster 1 closing and thruster 4 blocking.

behavior of the residuals and the decision test. As can be seen, the two faults are successfully detected and isolated.

Remark 2: It should be pointed out that the (a priori fixed) rejecting component at $\omega \approx 6.10^{-3}$ rad/s introduced within the residual generators induces a transient behavior of the residuals $r_i(t) = M_{y_i} y_j(t) + M_{u_i}(t) T_i(t) - L_i(s)(\frac{y_j}{T_i})$, $i = 1, \ldots, 12$, $j = 4, \ldots, 9$ that has been revealed to be about 4000 s. This may be questionable from a practical point of view, because it may lead to false alarms, for example, when an intermittent thruster fault occurs. In such a case, the solution may consist of judiciously combining the two proposed FDI schemes. For instance, one can design just one residual signal $\mathbf{r}(t)$ that is sensitive to all faults and robust against $h(\varpi_\alpha, \varpi_{\text{spin}})$ and n according to the method presented in Sec. III.A and combine it with the 12 residuals defined according to Eq. (41). A judgment fault is declared by a decision test applied to $\mathbf{r}(t)$, and the isolation task is fulfilled using the 12 residuals defined according to Eq. (41). Finally, we shall argue that such a reasoning vanishes if satellite onboard processors and hardware memories allow for the implementation of both the FDI schemes.

IV. Conclusions

This paper addressed the fault diagnosis task of the satellite Microscope thrusters. Microscope is a satellite that has the mission of testing the equivalence principle, which postulates the equality between gravitational mass and inertial mass with a resolution almost 3 orders of magnitude more than the best tests so far performed on Earth. Two FDI schemes based on H_∞/H_- filters are proposed to generate residuals robust against spatial disturbances (i.e., third-body disturbances, J_2 disturbances, atmospheric drag, and solar radiation pressure), measurement noises, and sensor misalignment phenomena while guaranteeing fault sensitivity performances. Nonlinear simulations show that, despite the fact that the considered faults are fully compensated by the control law, the faults are successfully detected and isolated.

References

[1] Chen, J., and Patton, R., *Robust Model-Based Fault Diagnosis for Dynamic Systems*, Kluwer Academic, Norwell, MA, 1999.

[2] Patton, R., Frank, P., and Clark, R., *Issues of Fault Diagnosis for Dynamic Systems*, Springer–Verlag, London, 2000, ISBN 3-540-19968-3.

[3] Venkatasubramanian, V., Rengaswamy, R., Yin, K., and Kavuri, S., "A Review of Process Fault Detection and Diagnosis. Part 1: Quantitative Model-Based Methods," *Computers and Chemical Engineering*, Vol. 27, No. 3, 2003, pp. 293–311.

[4] Blanke, M., Kinnaert, M., Lunze, M., and Staroswiecki, M., *Diagnosis and Fault Tolerant Control*, Springer–Verlag, New York, 2003.

[5] Isermann, R., "Model-Based Fault Detection and Diagnosis—Status and Applications," *Annual Reviews in Control*, Vol. 29, No. 1, 2005, pp. 71–85. doi:10.1016/j.arcontrol.2004.12.002

[6] Verma, V., Langford, J., and Simmons, R., "Non-Parametric Fault Identification for Space Rovers," *International Symposium on Artificial Intelligence and Robotics in Space*, June 2001.

[7] DeFreitas, N., "Rao–Blackwellised Particle Filtering for Fault Diagnosis," *Aerospace Conference Proceedings*, Vol. 4, IEEE Publications, Piscataway, NJ, 2002, pp. 1767–1772.

[8] Hutter, F., and Dearden, R., "Efficient On-Line Fault Diagnosis for Non-Linear Systems," *International Symposium on Artificial Intelligence, Robotics and Automation in Space*, May 2003.

[9] Dearden, R., Willeke, T., Simmons, R., Verma, V., Hutter, F., and Thrun, S., "Real-Time Fault Detection and Situational Awareness for Rovers: Report on the Mars Technology Program Task," *Proceedings of the IEEE Aerospace Conference*, IEEE Publications, New York, 2004, pp. 826–840.

[10] Venkateswaran, N., Siva, M., and Goel, P., "Analytical Redundancy Based Fault Detection of Gyroscopes in Spacecraft Applications," *Acta Astronomica*, Vol. 50, No. 9, 2002, pp. 535–545. doi:10.1016/S0094-5765(01)00209-0

[11] Jensen, H., and Wisniewski, R., "Fault Detection and Isolation for Spacecraft: Geometric Approach," *Proceedings of AIAA Guidance, Navigation and Control*, AIAA, Reston, VA, Aug. 2002.

[12] Edwards, C., Spurgeon, S., and Patton, R., "Sliding Mode Observers for Fault Detection and Isolation," *Automatica*, Vol. 36, No. 4, April 2000, pp. 541–553. doi:10.1016/S0005-1098(99)00177-6

[13] Tan, C., and Edwards, C., "Sliding Mode Observers for Robust Detection and Reconstruction of Actuator and Sensor Faults," *International Journal of Robust and Nonlinear Control*, Vol. 13, No. 5, Jan. 2003, pp. 443–446. doi:10.1002/rnc.723

[14] Edwards, C., and Thein, M., "Sliding Mode Fault Detection and Isolation in aSatellite Leader/Follower System," *Proceedings of IFAC SAFEPROCESS 2006*, International Federation of Automatic Control, 2006, pp. 367–372.

[15] Patton, R., Uppal, F., Simani, S., and Polle, B., "A Monte Carlo Analysis and Design for FDI of a Satellite Attitude Control System," *Proceedings of IFAC SAFEPROCESS 2006*, International Federation of Automatic Control, 2006, pp. 1393–1398.

[16] Nett, C., Jacobson, C., and Miller, A., "An Integrated Approach to Controls and Diagnostics: The 4-Parameter Controller," *Proceedings of ACC*, American Automatic Control Council, Dayton, OH, 1988.

[17] Murad, G., Postlethwaite, I., and Gu, D.-W., "A Robust Design Approach to Integrated Controls and Diagnostics," *Proceedings of the 13th Triennial World Congress*, International Federation of Automatic Control, 1996, pp. 199–204.

[18] Stoustrup, J., and Grimble, M., "Integrating Control and Fault Diagnosis: A Separation Result," *Proceedings of SAFE PROCESS 1997*, International Federation of Automatic Control, 1997, pp. 323–328.

[19] Stoustrup, J., Grimble, M., and Niemann, H., "Design of Integrated Systems for the Control and Detection of Actuator/Sensor Faults," *Sensor Review*, Vol. 17, No. 2, 1997, pp. 138–149. doi:10.1108/02602289710170311

[20] Khosrowjerdi, M., Nikoukhah, R., and Safari-Shad, N., "A Mixed H_2/H_∞ Approach to Simultaneous Fault Detection and Control," *Automatica*, Vol. 40, No. 2, 2004, pp. 261–267. doi:10.1016/j.automatica.2003.09.011

[21] Marcos, A., and Balas, G., "A Robust Integrated Controller/Diagnosis Aircraft Application," *International Journal of Robust and Nonlinear Control*, Vol. 15, No. 12, July 2005, pp. 531–551. doi:10.1002/rnc.1010

[22] Henry, D., and Zolghadri, A., "Design and Analysis of Robust Residual Generators for Systems Under Feedback Control," *Automatica*, Vol. 41, No. 2, Feb. 2005, pp. 251–264. doi:10.1016/j.automatica.2004.09.013

[23] Henry, D., and Zolghadri, A., "Design of Fault Diagnosis Filters: A Multi-Objective Approach," *Journal of the Franklin Institute*, Vol. 342, No. 4, 2005, pp. 421–446.

[24] Marcos, A., Ganguli, S., and Balas, G., "An Application of H_∞ Fault Detection and Isolation to a Transport Aircraft," *Control Engineering Practice*, Vol. 13, No. 1, Jan. 2005, pp. 105–119. doi:10.1016/j.conengprac.2004.02.006

[25] Mangoubi, R., Appelby, B., and Farrell, J., "Robust Estimation in Fault Detection," *Proceedings of the 31st Conference on Decision and Control*, IEEE Publications, Piscataway, NJ, 1992, pp. 2317–2322.

[26] Edelmayer, A., Bokor, J., and Keviczky, L., "H_∞ Detection Filter Design for Linear Systems: Comparison of Two Approaches,"

Proceedings of the 13th IFAC World Congress, International Federation of Automatic Control, 1996, pp. 37–42.

[27] Mangoubi, R., *Robust Estimation and Failure Detection: A Concise Treatment*, Springer–Verlag, Berlin/New York/Heidelberg, 1998.

[28] Rank, M., and Niemann, H., "Norm Based Design of Fault Detectors," *International Journal of Control*, Vol. 72, No. 9, 1999, pp. 773–783. doi:10.1080/002071799220704

[29] Collins, E., and Song, T., "Robust H_∞ Estimation and Fault Detection of Uncertain Dynamic Systems," *Journal of Guidance, Control, and Dynamics*, Vol. 23, No. 5, 2000, pp. 857–864.

[30] Stoustrup, J., and Niemann, H., "Fault Estimation—A Standard Problem Approach," *International Journal of Robust and Nonlinear Control*, Vol. 12, No. 8, 2002, pp. 649–673. doi:10.1002/rnc.716

[31] Stoorvogel, A., Niemann, H., Saberi, A., and Sannuti, P., "Optimal Fault Signal Estimation," *International Journal of Robust and Nonlinear Control*, Vol. 12, No. 8, 2002, pp. 697–727. doi:10.1002/rnc.714

[32] Castro, H., Bennani, S., and Marcos, A., "Robust Filter Design for a Re-Entry Vehicle," *Proceedings of the 7th International Conference on Dynamics and Control of Systems and Structures in Space*, 2006.

[33] Castro, H., Bennani, S., and Marcos, A., "Integrated Vs Decoupled Fault Detection Filter and Flight Control Law Designs for a Re-Entry Vehicle," *Proceedings of the 2006 IEEE International Conference on Control Applications*, IEEE Publications, Piscataway, NJ, 2006.

[34] Edelmayer, A., Bokor, J., and Szabo, Z., "Robust Detection and Estimation of Faults by Exact Fault Decoupling and H_∞ Disturbance Attenuation in Linear Dynamical Systems," *Proceedings of the 2006 American Control Conference*, 2006.

[35] Ding, S., Jeinsch, T., Frank, P., and Ding, E., "A Unified Approach to the Optimization of Fault Detection Systems," *International Journal of Adaptive Control and Signal Processing*, Vol. 14, 2000, pp. 725–745.

[36] Rambeaux, F., Hamelin, F., and Sauter, D., "Optimal Thresholding for Robust Fault Detection of Uncertain Systems," *International Journal of Robust and Nonlinear Control*, Vol. 10, 2000, pp. 1155–1173. doi:10.1002/1099-1239(20001215)10:14<1155::AID-RNC521>3.0.CO;2-V

[37] Hamelin, F., and Sauter, D., "Robust Fault Detection in Uncertain Dynamic Systems," *Automatica*, Vol. 36, No. 11, 2000, pp. 1747–1754. doi:10.1016/S0005-1098(00)00101-1

[38] Zhong, M., Ding, S., Lam, J., and Wang, H., "An LMI Approach to Design Robust Fault Detection Filter for Uncertain LTI Systems," *Automatica*, Vol. 39, No. 3, 2003, pp. 543–550. doi:10.1016/S0005-1098(02)00269-8

[39] Liu, J., Wang, J., and Yang, G., "An LMI Approach to Minimum Sensitivity Analysis with Application to Fault Detection," *Automatica*, Vol. 41, No. 11, Nov. 2005, pp. 1995–2004. doi:10.1016/j.automatica.2005.06.005

[40] Henry, D., and Zolghadri, A., "Norm-Based Design of Robust FDI Schemes for Uncertain Systems Under Feedback Control: Comparison of Two Approaches," *Control Engineering Practice*, Vol. 14, No. 9, 2006, pp. 1081–1097. doi:10.1016/j.conengprac.2005.06.007

[41] Jaimoukha, I., Li, Z., and Papakos, V., "A Matrix Factorization Solution to the H_-/H_∞ Fault Detection Problem," *Automatica*, Vol. 42, No. 11, Nov. 2006, pp. 1907–1912. doi:10.1016/j.automatica.2006.06.002

[42] Wied, B., *Space Vehicle Dynamics and Control*, AIAA, Reston, VA, 1998.

[43] Wisniewski, R., *Lecture Notes on Modelling of a Spacecraft*, Aldeling for Proceskontrol, Aalborg Universitet, Aalborg, Denmark, 2000.

[44] Jin, H., Wiktor, P., and DeBra, D., "An Optimal Thruster Configuration Design and Evaluation For Quick Step," *Control Engineering Practice*, Vol. 3, No. 8, 1995, pp. 1113–1118. doi:10.1016/0967-0661(95)00104-3

[45] Wiktor, P., "On-Orbit Thruster Calibration," *Journal of Guidance, Control and Dynamics*, Vol. 19, No. 4, 1996.

[46] Frank, P., Alcorta-Garcia, E., and Köppen-Seliger, B., "Modelling for Fault Detection and Isolation Versus Modelling for Control," *Mathematical and Computer Modelling of Dynamical Systems*, Vol. 7, No. 1, 2001, pp. 1–46.

[47] Massoumia, M., "A Geometric Approach to the Synthesis of Failure Detection Filters," *IEEE Transactions on Automatic Control*, Vol. 31, No. 9, 1986, pp. 839–846.